Imprinting Persistent Currents in Tunable Fermionic Rings

G. Del Pace,[1,*,†] K. Xhani,[1] A. Muzi Falconi,[2,1] M. Fedrizzi,[1] N. Grani,[1,3] D. Hernandez Rajkov,[1]
M. Inguscio,[4,1] F. Scazza,[2,1] W. J. Kwon,[1,‡] and G. Roati[1]

[1]*Istituto Nazionale di Ottica del Consiglio Nazionale delle Ricerche (CNR-INO) and European Laboratory
for Nonlinear Spectroscopy (LENS), University of Florence, 50019 Sesto Fiorentino, Italy*
[2]*Department of Physics, University of Trieste, 34127 Trieste, Italy*
[3]*Department of Physics and Astronomy, University of Florence, 50019 Sesto Fiorentino, Italy*
[4]*Department of Engineering, Campus Bio-Medico University of Rome, 00128 Rome, Italy*

Persistent currents in annular geometries have played an important role in disclosing the quantum phase coherence of superconductors and mesoscopic electronic systems. Ultracold atomic gases in multiply connected traps also exhibit long-lived supercurrents and have attracted much interest both for fundamental studies of superfluid dynamics and as prototypes for atomtronics circuits. Here, we report on the realization of supercurrents in homogeneous, tunable fermionic rings. We gain exquisite, rapid control over quantized persistent currents in all regimes of the BCS-BEC crossover through a universal phase-imprinting technique, attaining on-demand circulations w as high as 9. High-fidelity readout of the superfluid circulation state is achieved by exploiting an interferometric protocol, which also yields local information about the superfluid phase around the ring. In the absence of externally introduced perturbations, we find the induced metastable supercurrents to be as long-lived as the atomic sample. Conversely, we trigger and inspect the supercurrent decay by inserting a single small obstacle within the ring. For circulations higher than a critical value, the quantized current is observed to dissipate via the emission of vortices, i.e., quantized phase slips, which we directly image, in good agreement with numerical simulations. The critical circulation at which the superflow becomes unstable is found to depend starkly on the interaction strength, taking its maximum value for the unitary Fermi gas. Our results demonstrate fast and accurate control of quantized collective excitations in a macroscopic quantum system and establish strongly interacting fermionic superfluids as excellent candidates for atomtronics applications.

I. INTRODUCTION

In a conducting ring pierced by a magnetic field, the electronic wave functions are augmented by a phase winding enforced by the associated vector potential [1,2]. The most striking manifestation of such a geometric phase factor is the quantization of the magnetic flux enclosed by the loop into discrete values, inherently associated with the emergence of persistent diamagnetic currents around the ring [1–5]. In μm-sized metallic rings,

such persistent currents are the hallmark of mesoscopic physics, as they are underpinned by the electronic phase coherence throughout the entire system [6,7]. In superconducting or superfluid loops, characterized by macroscopic phase coherence [8], circulating supercurrents appear whenever particles experience a gauge field—which, in neutral matter, may be synthetically created [9,10]—as an outcome of the famous Aharonov-Bohm effect [11] and the continuity of the wave function around the loop. Supercurrents are extremely long-lived and are, for instance, exploited in the operation of superconducting high-field electromagnets with vanishing energy dissipation [12].

In neutral superfluids, such as helium or ultracold atomic condensates, metastable supercurrents [13,14] may also flow in the absence of a gauge field: Even though the ground state of a superfluid ring has zero current, a supercurrent can be excited, e.g., by externally imposing a dynamical phase gradient around the loop. Since the phase of the superfluid wave function must wind around the ring by an integer multiple of 2π, only discrete supercurrent states can exist [15], denoted by an integer winding number $w \neq 0$. States with different w are associated with

w-charged vortices enclosed in the superfluid. In multiply connected ring geometries, vortices are preferentially trapped inside the ring at vanishing density, and topologically distinct *w* states are thus separated by energy barriers [15]. As a result, excited *persistent* current states in superfluid rings are long-lived and generally insensitive to disorder, thermal fluctuations, and even particle losses.

Atomic persistent currents have been realized in weakly interacting Bose-Einstein condensates (BECs) confined in toroidal traps [16–18]. Studies of the long-time dynamics of persistent currents in BECs have revealed their metastable and quantized character [17], identifying quantized phase slips as the excitations connecting states with different winding numbers to each other [17,19,20]. Recently, long-lived single-winding ring currents were produced for the first time by stirring strongly interacting Fermi gases [21], and they were observed to survive even when the system was driven out of the superfluid phase and back. Yet, many open questions remain about the detailed physical processes governing the persistent current decay, especially in fermionic pair condensates where multiple excitation mechanisms may compete or cooperate with one another. For tightly confined rings, coherent and incoherent phase-slippage processes are thought to dominate the decay in different temperature and interaction regimes [22–25], sharing intriguing analogies with the glassy dynamics and avalanches observed in certain disordered systems [26].

Besides providing an important playground for the investigation of artificial quantum matter, ultracold atomic rings are also a promising platform for quantum technologies. An annular atomic superfluid embodies the minimal realization of a matter-wave circuit, providing an elementary building block for future atomtronics devices [27,28] and neutral current-based qubit implementations [29]. Persistent currents in ring condensates could be employed for quantum sensing, offering an atomtronics analogue of superconducting quantum interference devices (SQUIDs) [30–34] or new-generation inertial force sensors [35–37] thanks to the Sagnac effect. For any technological application, a high degree of control over persistent currents is essential; in particular, a rapid deterministic creation and a high-fidelity readout of the current state at the single quantum level are of utmost importance.

In this work, we realize fermionic superfluids in tunable, homogeneous ring traps in different regimes of the crossover from a molecular BEC to a Bardeen-Cooper-Schrieffer (BCS) superfluid, and we control their circulation at the single quantum level by optically imprinting an adjustable dynamical phase. By employing an interferometric probe to measure the winding number of the ring, we demonstrate our protocol to be effective throughout the crossover in creating on-demand supercurrents of tunable circulation. These states are observed to persist as long as the atomic sample does, demonstrating circulating currents to be particularly robust against particle losses. On the other hand, we promote the persistent current decay by inserting a local defect in the ring. Whereas we find low-circulation states to be insensitive to the introduced perturbation, for circulations higher than a critical value, we observe the supercurrent to decay via the emission of quantized vortices, which cause phase slippage leading to the reduction of the phase winding around the ring down to a lower stable value. The onset of dissipation is triggered when the lowest-lying excitations become energetically accessible, exposing the different characters of paired Fermi superfluids.

II. TUNABLE FERMIONIC RINGS

In our experiment, we produce fermionic superfluids of ^{6}Li atom pairs in different regimes across the BEC-BCS crossover by varying the interatomic *s*-wave scattering length *a* between the two lowest hyperfine states in the vicinity of a Feshbach resonance. We focus on three distinct superfluid regimes of a molecular BEC, a unitary Fermi gas (UFG) and a BCS superfluid with coupling strength $1/k_F a \simeq (3.6, 0, -0.4)$, where $k_F = \sqrt{2mE_F}/\hbar$ is the Fermi wave vector, with $\hbar = h/2\pi$ the reduced Plank constant, *m* the mass of the ^{6}Li atom, and $E_F/h \simeq \{8.2, 9.4, 9.0\}$ kHz the Fermi energy in the three regimes, respectively. The superfluid ring is realized by the combination of a tight harmonic confinement along the vertical direction and sculpted optical potentials in the *x*-*y* plane [Fig. 1(a)]. We adjust the harmonic vertical trap frequency ν_z to ensure a similar relative confinement of $h\nu_z/E_F \sim 0.05$ throughout all the explored interaction regimes, thus keep three dimensional our ring superfluid. The
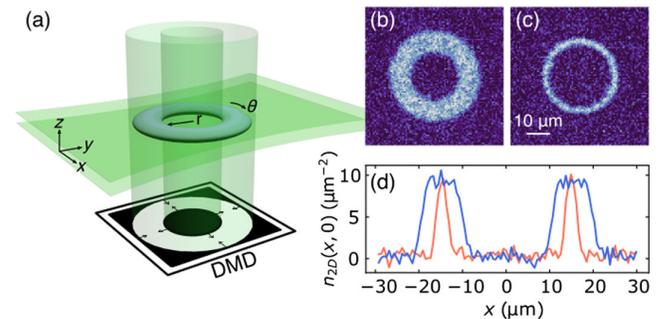
FIG. 1. Tunable homogeneous rings with ultracold fermionic superfluids. (a) Sketch of the experimental setup. A blue-detuned TEM$_{01}$-like beam propagates horizontally and provides a tight harmonic trap in the vertical *z* direction, whereas a DMD-made repulsive potential sculpts a tunable ring-shaped boxlike confinement in the *x*-*y* plane. The latter is imaged onto the atomic cloud by a high-resolution microscope objective, omitted in the figure. (b,c) *In situ* images of a unitary Fermi superfluid confined in two ring geometries with different radial thickness, comprising around 7.5×10^3 and 2.7×10^3 fermion pairs, respectively. The images correspond to a single experimental acquisition of the atomic density. (d) Density cuts along the $y = 0$ diameter of the rings in panels (b) and (c) are shown as blue and orange lines, respectively, obtained by averaging over 20 realizations.

ring-shaped trapping potential in the x-y plane is tailored by a digital micromirror device (DMD) illuminated with blue-detuned light to provide a repulsive optical potential. The DMD provides us the flexibility for arbitrarily tuning the superfluid ring geometry, both in terms of mean radius and thickness [Figs. 1(b) and 1(c)]. In particular, the latter can be reduced down to a Gaussian full width at half maximum (FWHM) of 2.7(1) μm in the radial direction [Fig. 1(c)], reaching similar conditions to those explored in Ref. [21]. In such geometry, the size of the ring becomes comparable with the typical size ξ_0 of fermionic pairs in the strongly interacting regime. At unitarity $\xi_0 \sim 1/k_F \simeq 0.3$ μm, and ξ_0 grows as $\xi_0 \simeq 1/k_F \exp(-\pi/2k_F a)$ toward the BCS limit, taking a value $\xi_0 \simeq 0.6$ μm at $1/k_F a = -0.4$. Even deeper in the BCS regime, the evolution of the superfluid phase around the ring would become essentially one dimensional in terms of the azimuthal spatial coordinate, allowing for future explorations of one-dimensional out-of-equilibrium dynamics [38,39].

Here, we concentrate our attention on the geometry of Fig. 1(b), which features internal and external radii of 10 and 20 μm, respectively, and comprises $N \simeq 7.5 \times 10^3$ superfluid pairs at a temperature of $T \simeq 0.4 T_c$, where T_c is the critical temperature for the superfluid transition in each regime. Given the high resolution of the DMD projection setup, the box-trap confinement results in a uniform density both along the azimuthal and the radial direction of the ring [Fig. 1(d)], limited by a steep wall with a height much larger than the chemical potential μ of the superfluid.

III. ON-DEMAND EXCITATION AND DETECTION OF SUPERCURRENTS

We excite nonzero circulation states by optically imprinting a dynamical phase on the ring. Optical phase imprinting has been demonstrated to be an effective technique to create solitons [40,41] and phase imbalance triggering Josephson oscillations [42], but it has not been employed to inject rotational excitations so far. We exploit the DMD to create an optical azimuthal gradient with uniform intensity across the radial direction [Fig. 2(c)], which we shine onto the superfluid ring for a short adjustable time t_I. When t_I is shorter than the characteristic density response time, i.e., $t_I < \hbar/\mu$, the light imprints a phase $\phi_I = U_0 \times t_I/\hbar$ onto the atomic wave functions [40,43], where U_0 is the spin-independent potential exerted by the light field on the atomic states. The imprinting effectively transfers the superfluid in one of the local minima of the parabolic washboard potential pictorially sketched in Fig. 2(b), i.e., into a metastable persistent current state [17,20]. In particular, in the absence of other excitations, when the imprinted phase difference at the gradient discontinuity $\Delta\phi_I$ equals $2\pi w$, a persistent current state with winding number w is excited,
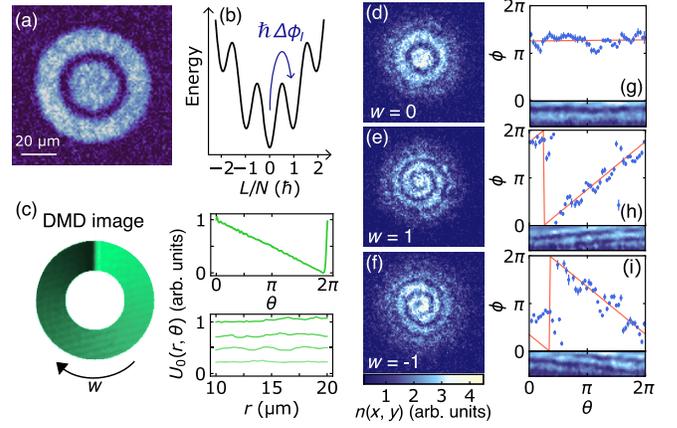
FIG. 2. Excitation and detection of the circulation state. (a) *In situ* image of the BEC superfluid in the trap configuration we employ to interferometrically probe the ring winding number. (b) Energy landscape of the ring superfluid as a function of the total angular momentum per pair L/N. The imprinting of an optical phase $\Delta\phi_I$ operates the transition into one of the metastable persistent current states at winding number w. (c) DMD-made light pattern, diagnosed by a secondary imaging camera, employed for the phase imprinting and corresponding light shift U_0. In the top panel, $U_0(\theta)$ is averaged along the radial direction in the ring; in the bottom panel, $U_0(r)$ is averaged over 0.07 rad across $\theta = 0, \pi/2, \pi, 3\pi/2$ for decreasing line intensity, respectively. The sharp opposite gradient at $\theta \simeq 2\pi$ has a dimension of $\Delta\theta = 0.15$ rad. (d)–(f) Interferograms of the BEC superfluid, obtained from a single absorption image after a TOF expansion of 1.2 ms without phase imprinting (d) and with a phase imprinting of $\Delta\phi_I \simeq 2\pi$ in the clockwise (e) and anticlockwise (f) directions. (g)–(i) Fit of the local relative phase ϕ extracted from the interferograms. After changing the image into polar coordinates (bottom panel), a sinusoidal fit of each azimuthal slice of the interferogram is performed to extract ϕ as the relative phase shift (blue dots on top panels). The polar images comprise the radial region at 1.5 μm $< r < 12$ μm, cut into 100 azimuthal slices. Symbols (error bars) in the (g)–(i) top panels represent the weighted average (weighted standard deviation) over the fitted values of ϕ and their 1σ uncertainty of the fit in bins of 0.125 rad size. A linear fit (red solid lines) provides a measurement of the winding number as the slope of the $\phi - \theta$ curve. We obtain $w = 0.01(2)$, $w = 1.00(9)$, and $w = -0.99(9)$ for panels (g)–(i), respectively.

characterized by a velocity $v = w\hbar/2mr$ and an angular momentum per superfluid pair $L/N = w\hbar$.

To measure the winding number, we carry over to fermionic superfluids the interferometric technique previously demonstrated for weakly interacting BECs [44–46]. In analogy to self-heterodyne detection in optics, we exploit a central disk condensate as a local oscillator to provide a constant phase reference [Fig. 2(a)], and we observe the fringe pattern arising after interfering it with the ring during a time-of-flight (TOF) expansion. In the strongly interacting regime, the resulting interference is detected after having tuned a to adiabatically transfer the

superfluid into a molecular BEC. When the superfluid ring is prepared at rest (see Appendix A for further details), the interferogram displays fringes arranged as concentric rings [Fig. 2(d)], revealing an azimuthally uniform phase difference between the two condensates. On the other hand, when a state with finite w is excited in the ring, the interferogram changes into a spiral fringe pattern [Figs. 2(e) and 2(f)], reflecting the linear trend of the wave-function phase around the ring. In particular, the spiral direction discloses the sign of the winding number w, while the number of arms measures its magnitude [44]. The interferometric detection allows us to quantitatively access the circulation of fermionic superfluid rings, which so far has been probed only by detecting the presence of vortices after a TOF expansion [21]. Moreover, the high resolution of the obtained interferograms allows us to extract local information on the relative phase ϕ between the ring and the disk condensates [45]. By switching from Cartesian to polar coordinates [Figs. 2(g)–2(i), bottom] and performing a sinusoidal fit on each azimuthal slice of the interferogram [47], we obtain a $\phi - \theta$ curve [Fig. 2(g)–2(i), top] whose slope measures the winding number. The local imaging of the superfluid-ring azimuthal phase provides an unparalleled resource for future investigations, especially in tightly confined rings. For example, one could investigate the local phase evolution and its fluctuations around the ring when perturbations are added [44,46], when multiple rings are coupled together [48–50], or look for phase dislocations, which are expected to characterize the interferograms acquired in the strongly interacting regime [51].

IV. PERSISTENT CURRENTS ACROSS THE BEC-BCS CROSSOVER

By imprinting the superfluid phase and reading out the winding number via the interferograms, we gain accurate control over the circulation state of the rings, which we tune by acting on the imprinting parameters. In Fig. 3(a), we report the measured mean winding number $\langle w \rangle$ averaged over several experimental realizations of the same imprinting procedure, in the three interaction regimes, as a function of $\Delta\phi_I$. In all superfluids, $\langle w \rangle$ displays a steplike trend, consistent with previous observations with bosonic ring superfluids [17,19] and with Gross-Pitaevskii equation (GPE) numerical simulations at zero temperature of our imprinting protocol (dashed line) [47]. Both numerical and experimental BEC data show that $\Delta\phi_I \simeq 2\pi w$ is needed to deterministically excite the circulation state of winding number w, but they also show that a lower imprinted phase is enough to populate it (see Appendix B for further details). The switching between $w = 0$ and $w = 1$ is observed to occur for a slightly larger imprinted phase in the BEC experimental data with respect to GPE results. This is likely due to the collective soundlike excitations that unavoidably affect the superfluid as a consequence of the (optically imperfect) imprinting pulse and show a more
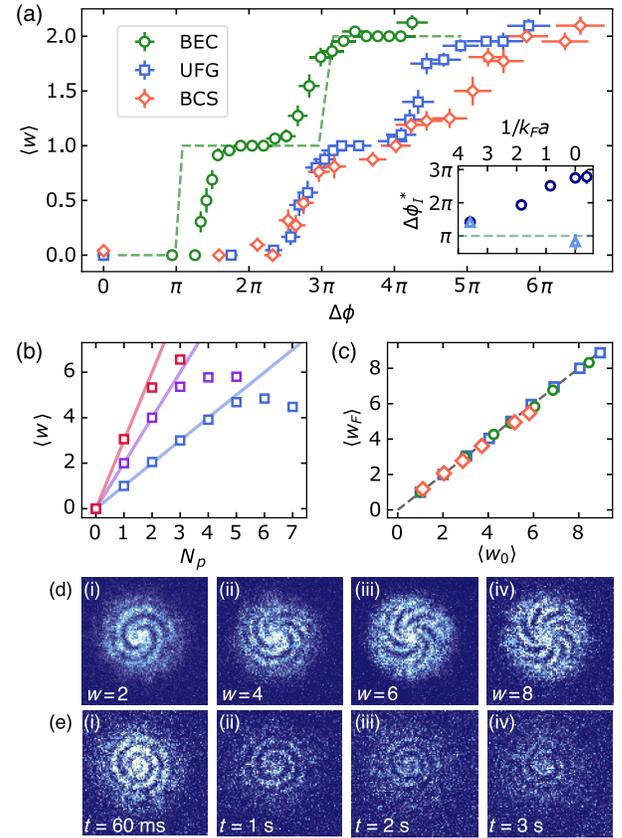
FIG. 3. Persistent currents with on-demand circulation in the BEC-BCS crossover. (a) Average winding number $\langle w \rangle$, measured over 20 interferograms acquired after the imprinting of a phase jump $\Delta\phi_I$ for the three interaction regimes of $1/k_F a \simeq \{3.6, 0, -0.4\}$, labeled as BEC, UFG, and BCS, respectively. The interferograms are acquired 60 ms after the end of the imprinting pulse. All data sets are obtained by varying the imprinting time at constant U_0 in each regime. The green dashed line represents GPE numerical simulations of our imprinting protocol, performed under the same experimental conditions of the BEC superfluid. Inset: imprinted phase jump $\Delta\phi_I^*$ (see text) as a function of the interaction strength for simple gradient imprinting (dark blue circles) and modified by adding a barrier at the discontinuity (light blue triangles). The gray dashed line marks $\Delta\phi_I^* = \pi$, as expected from GPE numerical simulation. Vertical error bars denote the standard error of mean (SEM); horizontal ones are instead obtained by considering the experimental uncertainty of 5% in the U_0 calibration. (b) Average circulation of a unitary superfluid measured after a variable number N_p of identical imprinting pulses of $w_i = 1$ (blue), 2 (purple), and 3 (red) each separated 10 ms from the following. The solid lines represent the linear scaling of $\langle w \rangle = w_i \times N_p$. (c) Average circulation $\langle w_F \rangle$ measured after a long time evolution of the initially imprinted state $\langle w_0 \rangle$ for the three interaction regimes [same notation as in panel (a)]. We measure $\langle w_0 \rangle$ and its SEM 60 ms after the imprinting pulse and $\langle w_F \rangle$ after 1.5 s for $\langle w_0 \rangle \leq 3$, after 1 s for $3 < \langle w_0 \rangle \leq 6$, and after 0.5 s for $\langle w_0 \rangle > 6$ in the BEC and UFG regimes. For BCS superfluids, $\langle w_F \rangle$ is measured after 1 s and 0.5 s for $\langle w_0 \rangle \leq 3$ and $\langle w_0 \rangle > 3$, respectively. (d) Interferograms of high circulation states, acquired for BCS (i, ii) and UFG (iii, iv) superfluids 60 ms after the last imprinting pulse. (e) Interferograms of the unitary superfluid in the $w = 1$ state as a function of time after the imprinting pulse. Images in (d) [(e)] consist of the average of two [single] independent experimental acquisitions.

pronounced effect in experiments with respect to simulations, possibly due to finite temperature. In fact, we observe that immediately after an imprinting pulse of any duration, the density of the superfluid is depleted at the location of the optical gradient discontinuity (see Appendix C for further details). We ascribe such a density depletion to a steep, yet not infinitely sharp, intensity gradient in the opposite direction [Fig. 2(c)], due to the finite resolution of about 1 μm of our imaging system. Even though the presence of such an antigradient has been postulated to completely prevent phase imprinting to populate persistent current states at finite circulations [43], its particularly small spatial extension in our case leads to density excitations that decay over a timescale of a few ms into sound waves or vortices. The vortices nucleated after the imprinting are observed to survive on top of the macroscopic current for a few hundreds of ms, without perturbing the generated persistent current state, consistent with previous observations in stirred bosonic superfluids [19].

In the strongly interacting regime, even though the steplike trend of Fig. 3(a) is preserved with a comparable size of the plateaus at nonzero $\langle w \rangle$, we observe that a larger $\Delta\phi_I$ is required to excite the $w = 1$ state. We quantitatively estimate such a shift by fitting the first step of the $\langle w \rangle - \Delta\phi_I$ curves with a sigmoidal function to extract the imprinted phase jump $\Delta\phi_I^*$ necessary to populate the $w = 1$ state with 50% probability. As reported in the inset of Fig. 3(a) in dark blue circles, $\Delta\phi_I^*$ is observed to monotonically increase with decreasing $1/k_F a$. By monitoring the short time dynamics after the imprinting of $\Delta\phi_I = 2\pi$ in the strongly interacting superfluid at $1/k_F a \simeq 0.9$, we observe that the azimuthal phase winding is actually imprinted, confirming the effectiveness of the protocol, but that it quickly decays out in a few ms (see Appendix C for further details). An imprinted $\Delta\phi_I = 2\pi$ is thus not able to populate the $w = 1$ state, and the imprinted angular momentum is dissipated into other excitations, probably those triggered by the sharp antigradient, which might have a more dramatic effect as we tune the interactions towards the BCS regime, as observed for the imprinting of solitons [52]. To confirm this, we test the imprinting protocol in the BEC and UFG superfluids after modifying the DMD image by inserting a repulsive optical barrier in correspondence with the gradient discontinuity, as suggested in Ref. [53], to circumvent the destructive effect of the antigradient on the imprinted current. In this case, we observe the $\langle w \rangle - \Delta\phi_I$ curves in the two interaction regimes to provide a $\Delta\phi_I^*$ almost comparable with the one expected by GPE simulation [light blue triangles in Fig. 3(a), inset]. Removing the sharp light gradient allows us to drastically reduce the unwanted density excitation produced by the imprinting, yet it leads to a degraded fidelity of only 90% for the initialization of the $w = 1$ state, likely resulting from the interaction between the moving superfluid and the barrier during the imprinting time [53]. For this reason, we choose

the simple gradient imprinting procedure, which is best suited to deterministically excite nonzero circulation states even in the strongly interacting regime. Although previous theoretical and numerical studies pointed out the incapability of the phase imprinting of a simple azimuthal gradient in exciting finite winding numbers in atomic annular superfluids [43,53], our results demonstrate it as an effective and versatile method to access on-demand w states. For this method to work, a high-resolution optical pattern is necessary to limit the pollution introduced by the sharp gradient in the opposite direction.

Through the phase imprinting protocol, we populate the metastable state at $w = 1$ with a reproducibility greater than 99% in both BEC and unitary regimes, whereas we obtain a few-percent lower fidelity in the BCS case. Higher-w states can then be excited by increasing the imprinting pulse duration. However, in all superfluid regimes, we observe that, for increasing t_I, the probability to populate a well-defined w decreases, while the measured average winding number saturates at about $\langle w \rangle \simeq 6$, in agreement with GPE numerical simulations [47]. For increasing imprinting time, the more dramatic density excitations that follow the imprinting favor the nucleation of additional vortices from the innermost ring boundary, removing circulation quanta from the current and thus setting a limit for the highest w that we can populate. To access even higher w states, we keep $t_I \lesssim 500$ μs and rather increase the number of imprinting pulses. Figure 3(b) demonstrates the scalability of our imprinting protocol; i.e., the addition of consecutive pulses of a given imprinting time (different colors) produces a linear increment on the measured $\langle w \rangle$. Even though the multiple phase imprinting protocol becomes ineffective for more than 4–5 pulses, this method still surpasses the single-pulse one, allowing us to access up to $w_{max} = \{8, 9, 6\}$ in the BEC, UFG, and BCS regimes, respectively [Figs. 3(c) and 3(d)]. The whole imprinting procedure takes up to 30 ms when we employ 3 pulses to access $w \geq 5$, demonstrating the multiple pulse scheme as a route to excite high circulation states much more rapidly than with stirring protocols [19], as employed in Ref. [21] to excite persistent currents in fermionic superfluids. By monitoring the time evolution of the interferograms in all superfluid regimes at long times after the last imprinting pulse, we verify that the imprinted circulation produces a persistent current of constant mean winding number $\langle w \rangle$, which is observed to be as long-lived as the superfluid sample. In particular, the $w = 1$ current is observed to persist up to 3 s with $\langle w \rangle > 99\%$ at unitarity, unaffected by the progressive decrease in atom number [Fig. 3(e)]. Circulations higher than w_{max} are also accessible via phase imprinting, but they undergo a decay towards states at smaller w in a few-tens-of-ms timescale [47]. The maximum stable persistent current w_{max} accessible under our experimental conditions corresponds to superfluid velocities at the inner ring radius of 4.2 mm/s, 4.8 mm/s, and 3.2 mm/s for $w = 8$, $w = 9$,
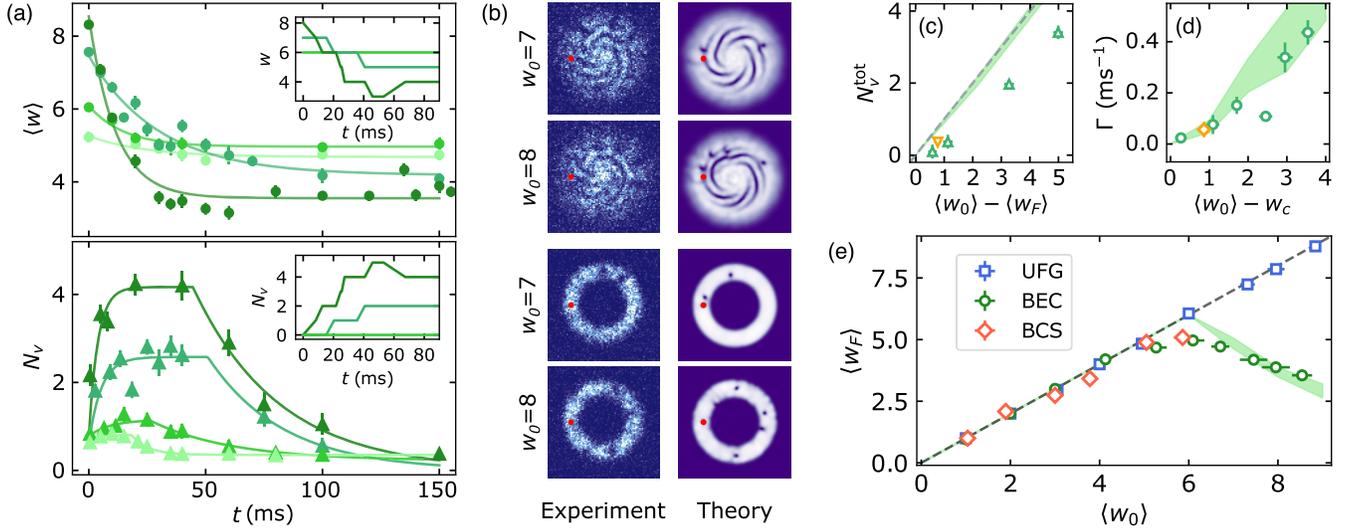
FIG. 4. Persistent current stability in the presence of a local perturbation. (a) Average circulation $\langle w \rangle$ and number of vortices N_v measured after a time t from the introduction of a controlled point defect in the ring BEC superfluid ($1/k_F a \simeq 3.6$). Symbols with the same color share equal starting experimental conditions; darker shades of green correspond to higher initial circulation. Data in the bottom panel are acquired by ramping up the optical defect 300 ms after the excitation of the persistent current, to have on average less than one vortex generated by the imprinting remaining in the ring. Solid lines represent an exponential fit for $\langle w \rangle$, and an exponential charging and discharging fit for N_v. Insets: GPE numerical simulation results of the same quantities, plotted using the same color convention. (b) Comparison between experimental and GPE simulated interferograms (top) and simple ring TOF (bottom) in the presence of the defect. The position of the defect is marked by a red dot in each image. Experimental interferograms are obtained at $t = 20$ ms, and the numerical ones at $t = 40$ ms and $t = 28$ ms for $w_0 = 7$ and $w_0 = 8$, respectively. The experimental (numerical) images of vortices in the ring are obtained for $t = 5$ ms and $t = 40$ ms ($t = 24$ ms and $t = 53$ ms) for $w_0 = 7$ and $w_0 = 8$, respectively. The time shift between experimental and numerical images of vortices accounts for the 13-ms time interval taken to remove the obstacle in the experiment. (c,d) Fitted values of the total number of emitted vortices N_v^{tot} and winding number decay rate $\Gamma = A/\tau$, where A is the amplitude and τ the decay time from the exponential fit, for BEC (green symbols) and $1/k_F a \simeq -0.4$ BCS (orange symbols) superfluids. The gray dashed line in panel (c) marks $N_v^{\text{tot}} = \langle w_0 \rangle - \langle w_F \rangle$. (e) Stability of the circulation for fermionic superfluids (see legend) in the presence of a local defect of height $V_0 \simeq 0.1 E_F$ in a BEC and $V_0 \simeq 0.2 E_F$ in unitary (UFG) at $1/k_F a \simeq 0$ and BCS superfluids. For $\langle w_0 \rangle > w_c$, the final winding number $\langle w_F \rangle$ is obtained from the exponential fit of the current decay, whereas for $\langle w_0 \rangle \leq w_c$, it simply represents the measured average circulation at $t \geq 150$ ms. In panels (c)–(e), the results obtained from an exponential fit of the GPE numerical simulations are reported as green shaded regions. Error bars in panel (a) denote the SEM, while in panels (c)–(e), they represent the 1σ uncertainty of the fit.

and $w = 6$ in the BEC, UFG, and BCS regimes, respectively, to be compared with the peak sound speed, estimated as $c_s \simeq \{5.8, 14.1, 14.4\}$ mm/s, respectively [47]. In all regimes, the superfluid velocity at w_{max} is observed to be lower than c_s, likely due to the excitations introduced by each imprinting pulse, which effectively set an upper bound for the winding number of the persistent current even for the multiple pulse procedure. In this framework, the relatively lower w_{max} observed in the BCS superfluid is consistent with pair-breaking excitations lowering the critical velocity for vortices to enter the superfluid ring, effectively reducing the current winding number. As a reference, the critical velocity associated with pair breaking takes a value of roughly 9 mm/s at $1/k_F a = -0.4$ [47].

V. STABILITY OF SUPERCURRENTS AGAINST A POINTLIKE DEFECT

To further investigate the connection between persistent currents and vortices arising from their common

topological nature, we foster vortex nucleation by introducing a controlled optical defect along the ring. After having excited a desired circulation state w_0, we introduce an approximately round obstacle with FWHM = 1.6 μm and height $V_0 \approx 0.1 E_F$ for the BEC superfluid, positioned in the midst of the inner and outer edges of the ring trap (see Appendix A for further details). The small defect size, comparable with the characteristic length of the superfluids, is not sufficient to cut the superflow in the radial direction but rather acts as a local perturbation to the current. By monitoring the time evolution of interferograms as a function of the holding time t in the presence of the defect, we track the average winding number evolution, as reported in Fig. 4(a) for the BEC superfluid. In particular, we observe that the defect has no effect on the current up to a critical winding number $w_c = 5$, whereas it induces a current decay for $w > w_c$. In the latter case, the interferograms directly display the presence of vortices in the superflow, as reported in Fig. 4(b). We quantitatively study the defect-induced emission of vortices by monitoring the

TOF expansion of the ring superfluid only [Fig. 4(b)], after having ramped down the obstacle, and by counting the number of vortices N_v as a function of the holding time [Fig. 4(a)]. After a fast growth, N_v saturates to a value that increases with w_0 and then decays again as vortices travel outside from the superfluid density. The whole dissipative dynamics develops in a timescale of hundred ms, as a result leaving a lower, yet stable current of circulation $w < w_0$ and no vortices.

To gain more insight into the defect-induced vortex emission dynamics, we perform GPE numerical simulations of the current decay, monitoring the time evolution of the interferograms [Fig. 4(b), left column]. Similarly to the experimental results, numerical simulations involve a critical circulation $w_c = 6$ for the stability of the current [Fig. 4(a)], above which vortices enter into the superfluid bulk causing the global current to decay [Fig. 4(b)]. For $w > w_c$, the numerical density profiles of the superfluid ring reveal that the defect favors the emergence of a low-density channel, which links it to the inner edge of the ring (see Appendix B for further details). Here, the local velocity of the superfluid is observed to increase until it exceeds the local speed of sound and fosters the nucleation of vortices into the bulk [54]. Each vortex removes one circulation quantum from the ring current; i.e., it induces the phase around the ring to slip by 2π, provoking the current decay as soon as it enters the superfluid density [Fig. 4(a), inset in bottom panel]. We note that, contrarily to the experimental data, the detected number of vortices in the numerical interferograms does not decay at long times t. Such a discrepancy is likely due to the finite temperature of the experimental system, which is expected to accelerate the vortex escape from the ring density, especially during the interaction with the defect, after completing one turn of the ring.

We perform exponential fits of the decay of $\langle w \rangle$ and the growth of N_v, parametrizing the observed dynamics in terms of the circulation decay rate Γ, the final average circulation $\langle w_F \rangle$, and the total number of emitted vortices N_v^{tot} [Figs. 4(c)–4(e)]. Consistently with a current decay given by vortex nucleation, the total number of emitted vortices is observed to increase with the total drop of the winding number, $\langle w_0 \rangle - \langle w_F \rangle$. Because of technical limitations of the experimental procedure to detect vortices, the measured N_v^{tot} is systematically lower than $\langle w_0 \rangle - \langle w_F \rangle$, whereas numerical simulations show a one-to-one correspondence between the two quantities (shaded region). Furthermore, both in experiments and GPE numerical simulations, higher circulations are observed to decay faster and to lower $\langle w_F \rangle$. In particular, Γ shows a monotonically increasing trend as a function of $\langle w_0 \rangle - w_c$, reminiscent of the linear scaling of the vortex shedding frequency with the velocity of a moving obstacle in a superfluid at rest [55–57]. However, a comparison with vortex shedding phenomena should be done carefully, as

the superflow velocity in our case is not constant over time because of vortices entering the ring density, and it is higher on the side of the defect facing the inner edge of the ring. Such an asymmetry plays an essential role in the microscopic route to vortex nucleation, as under our experimental conditions a single vortex per time enters the superfluid bulk rather than a vortex dipole as for shedding protocols [56,57].

We investigate the effect of the local perturbation on the current in the strongly interacting superfluids as well, changing its height to $V_0/E_F \simeq 0.2$, corresponding to the lowest value of V_0 experimentally accessible in this regime (see Appendix A). Figure 4(e) shows the comparison between the defect-induced current decay in the different superfluid regimes. Similarly to the BEC superfluid, the BCS superfluid presents a critical circulation of $w_c = 5$, whereas we observe no decay for any of the accessible currents in the UFG superfluid. Also in the BCS superfluid, the current decay is observed to proceed along with the entrance of vortices in the ring density, which happens over a timescale similar to that of the BEC regime [orange symbol in Figs. 4(c) and 4(d)], suggesting a similar decay dynamics. However, given the higher sound speed c_s in the BCS superfluid, the current decay is observed to happen for a smaller relative velocity at the inner ring radius, namely, corresponding to $0.18c_s$, instead of $0.46c_s$ as in the BEC. This gap is hardly explained by the different V_0 used in the two regimes, as we numerically verified that w_c in BEC superfluids only slightly changes upon increasing $V_0 > 0.1E_F$. Furthermore, for the same defect height, in the BCS regime, w_c is observed to be much smaller than for the UFG superfluid, despite the relatively small difference in $1/k_F a$ and expected c_s. Such observations are consistent with pair-breaking excitations lowering the critical velocity for vortex nucleation, as suggested also by the lower $w_{\max}$ measured in the BCS superfluid and by previous measurements of the vortex shedding critical velocity in fermionic superfluids [57]. On the other hand, the UFG superfluid shows the highest critical circulation in absolute value, even for a relatively higher obstacle with respect to the BEC superfluid, consistent with the expected higher chemical potential and critical velocity at unitarity.

VI. CONCLUSIONS AND OUTLOOK

In this work, we have realized tunable fermionic superfluid rings and gained a high degree of control over their persistent current states. We have demonstrated a fast protocol to populate on-demand winding numbers via optically imprinting the superfluid phase, which–contrarily to other phase-imprinting techniques based on the angular-momentum transfer from Laguerre-Gauss beams via Raman transitions [17,30]—is suitable for application with any atomic species. Furthermore, we applied an interferometric probe to measure the winding number of the ring fermionic superfluids, which we found to provide reliable

and local information on the phase around the ring. These capabilities may be exploited in the future to explore more complicated geometries, such as double rings tunnel-coupled through a thin barrier to investigate the circulation tunneling [48,49,58,59], or even ring lattices [50]. In particular, a coplanar tunnel-coupled double-ring system would realize the prototype of an atomtronics switch, implementing the atomic analog of a Mooji-Harmans qubit [49,60].

Furthermore, our work provides the first observation of persistent currents with high winding number in strongly interacting Fermi superfluids and the first study of their decay induced by a localized obstacle. In the clean system, we observed the current to be robust against particle losses and as long-lived as the atomic sample. By studying the higher winding number accessible under our experimental conditions, and the critical current in the presence of the defect, we exposed the intimate connection between persistent currents and vortices, namely, superfluid excitations united by the same topological character. In both cases, we observed the supercurrent breakdown to ensue at different critical values across the BEC-BCS crossover, as a consequence of the different dominant excitations—sound or pair-breaking—in different regimes. A direct extension of our work would be to probe the stability of the current in the presence of multiple defects and eventually in disordered potentials. Moreover, unitary superfluid currents have proven to be particularly robust against defects, suggesting strongly interacting Fermi superfluids as good candidates for applications in quantum sensing, such as atomic gyroscopes, where interactions are expected to enhance their sensitivity [61].

APPENDIX A: EXPERIMENTAL METHODS

1. Superfluid ring preparation

To create superfluid rings at rest, we start by preparing a homogeneous circular trap as in Ref. [62], complemented by a straight barrier across its diameter to hinder the spontaneous excitation of circulating currents in the subsequently created ring [Fig. 5(a1)]. We then ramp up the circular barrier, which creates the configuration shown in Fig. 2(a), used for the interferometric probing of the current
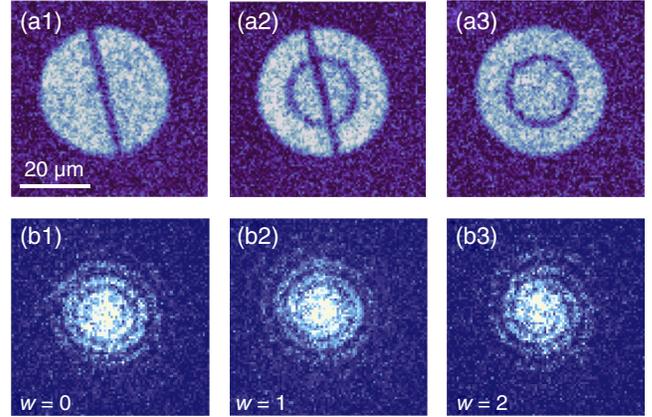
FIG. 5. (a1)–(a3) Experimental procedure to create superfluid rings in the $w = 0$ state. The whole trap preparation takes around 130 ms. Images are obtained as individual *in situ* absorption images of a unitary Fermi gas at different times during the trap loading sequence. (b1)–(b3) Interferograms for the ring geometry in Fig. 1(c) for different optically imprinted winding numbers $w = 0, 1, 2$. Each panel represents a single absorption image of the experimental sample.

states; once this has reached the final height [Fig. 5(a2)], we ramp down the straight barrier [Fig. 5(a3)]. Such a procedure allows us to trap fermionic superfluids at rest in rings of different widths and radii, which we can tune by suitably changing the dimensions of the repulsive potentials. For the thinnest ring geometries [Fig. 1(c)], we initially load a wider ring and subsequently squeeze it by enlarging the inner radius. This procedure allows us to trap a large number of atoms in the ring, yielding a clear signal in the interferograms used to determine the supercurrent winding number [Figs. 5(b1)–(b3)]. In particular, we demonstrate that in the thinnest ring geometry, we can deterministically excite the $w = 1$ and $w = 2$ states [Figs. 5(b2) and 5(b3)], which are observed to persist for several hundreds of ms.

We prepare ring superfluids in the different interaction regimes following the same procedure described in Ref. [62]. The thermodynamic properties of the superfluids throughout the BEC-BCS crossover are calculated by employing an analytical calculation in the hybrid trap, i.e., harmonic along the z direction and homogeneous in the x-y plane, based on the polytropic expansion and reported as Supplemental Material [47]. We note that a residual magnetic harmonic trap is present in the x-y plane, but its low trapping frequency of 2.5 Hz produces a negligible effect on the superfluid density. The Fermi energy is given by $E_F = 2\hbar\sqrt{\hbar\omega_z N/m(R_{out}^2 - R_{in}^2)}$, where $\omega_z \simeq 2\pi \times \{396, 523, 529\}$ Hz is the vertical trap frequency in the BEC, UFG, and BCS regimes, respectively, and $N = 7.5 \times 10^3$ is the number of atoms in the ring of internal and external radii of $R_{in} = 10$ μm and $R_{out} = 20$ μm. According to the same formulation, the pair chemical
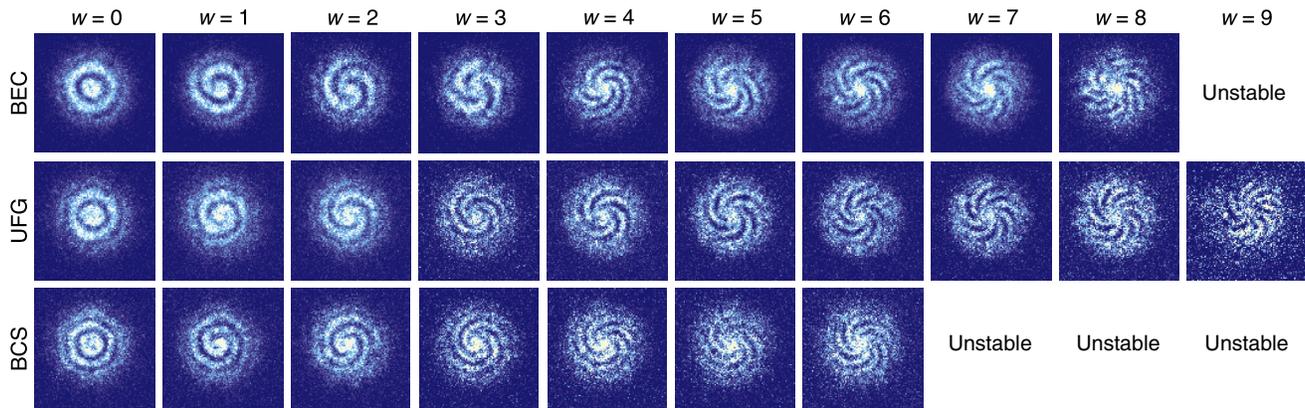
FIG. 6. Interferograms across the BEC-BCS crossover, acquired after a 1.2-ms TOF expansion. Images are obtained by averaging 2–4 single experimental shots. The color scales in the rows are normalized differently to compensate for the lower interference contrast in UFG and BCS superfluids.

potential takes the values of $\mu/h = \{1.0, 8.9, 10.0\}$ kHz, in the BEC, unitary, and BCS regimes, respectively [47]. These energy scales set the characteristic time and length to $\hbar/\mu \simeq 160$ μs, $\xi = \hbar/\sqrt{2m_P\mu} \simeq 0.64$ μm in the BEC regime, with $m_P = 2m$ the mass of a pair, $\hbar/\mu \simeq 18$ μs, and $1/k_F \simeq 0.30$ μm at unitarity, and $\hbar/\mu \simeq 16$ μs and $1/k_F \simeq 0.31$ μm in the BCS regime. We estimate the pair-breaking velocity as $v_{\rm pb} = [(\sqrt{\Delta^2 + \mu^2} - \mu)/m]^{1/2}$ [63,64], where $\Delta = 8/e^2 E_F \exp(\pi/2k_Fa)$ is the pairing gap [65]. In the UFG and BCS regimes, we acquire interferograms after having adiabatically swept the scattering length towards the BEC regime in 50 ms. We verify that such a sweep does not affect the ring current by checking that, without any imprinting, the interferograms always measure $w = 0$. For probing the $w > 8$ state at unitarity, we employ instead a fast 3.8-ms ramp of the magnetic field to prevent the current from decaying during the sweep to BEC, where $w_{\rm max} = 8$ [47]. A gallery of interferograms at different w in the three interaction regimes is reported in Fig. 6.

2. Light-pattern creation

All the repulsive optical potentials—which we employ for the creation of the ring trap, the realization of the phase imprinting, and the introduction of the local defect in the current flow—are obtained by shaping the intensity profile of a 532-nm blue-detuned laser beam with a DMD. These optical potentials are focused on the atomic cloud through the high resolution (~ 1 μm) imaging system described in Ref. [66]. The DMD also allows for a dynamical control of the potential, which we employ in the sample preparation described above, for the phase imprinting and for ramping up and down the obstacle. To create the gradient light profile of Fig. 2(c), we employ the feedback protocol described in Ref. [66]. The feedback effectively compensates for the Gaussian profile of the laser beam, producing a radially homogeneous and azimuthally linear light profile.

The sharp gradient in the opposite direction originates instead from the finite resolution of our imaging system, and the feedback procedure cannot correct it. Each imprinting pulse is realized by turning on the gradient profile in the DMD image for a variable time $t_I \geq 50$ μs, a limit set by the frame rate of the device. In particular, to populate the $w = 1$ state, we employ $t_I \simeq (130, 150, 170)$ μs for BEC, UFG, and BCS superfluids, respectively. We cannot exclude that the working condition of $t_I > \hbar/\mu$ could contribute to the more dramatic effect of the imprinting pulse in the strongly interacting regime that produces the shift in the $\langle w \rangle - \Delta\phi_I$ curve of Fig. 3. We verify at unitarity that increasing the overall gradient height to reduce the imprinting time needed to populate the $w = 1$ state down to $\simeq 110$ μs does not affect the $\langle w \rangle - \Delta\phi_I$ curve shift. These conditions correspond to the lowest t_I, i.e., the highest gradient height, accessible by our experimental constraints. We note that, for a given t_I, each imprinting pulse adds the ring superfluid wave function of exactly the same phase profile, which results in an identical spiral pattern in the interferogram. Thanks to the high reproducibility of the experimental sequence, interferograms obtained under the same condition can be averaged together to increase the fringe contrast.

The obstacle employed in Sec. V is realized by a 4×4 cluster of DMD mirrors, gradually turned on to ramp up its intensity (see Ref. [47] for details on the defect characterization). In particular, the ramp-up sequence is initiated 30 ms after the last imprinting pulse and lasts 13 ms. Once the obstacle has reached the final height, it is hold until the end of the experimental cycle for the BEC superfluid, while for the UFG and BCS superfluids, it is ramped down during the sweep towards the BEC regime to acquire the interferograms. The fact that both the obstacle and the ring trap are realized via the DMD imposes a constraint to the obstacle height in the strongly interacting regime. In particular, $V_0/E_F = 0.2$ corresponds to the lowest laser power

impinging on the DMD to be able to trap 7.5×10^3 atoms in the ring in the BCS regime.

3. Vortex detection

We quantitatively track the vortex nucleation induced by the presence of the defect described in Sec. V by imaging the superfluid density after TOF expansion of the ring only. For this purpose, we directly load the superfluid in a simple ring trap, added by a repulsive barrier in $\theta = 0$ to prepare it in $w = 0$. We excite the desired w_0 by employing the same imprinting scheme as for the winding number decay measurement and wait 300 ms to make sure the vortices created by the imprinting pulse have traveled out of the ring density. We then ramp-up the defect with the procedure already described, hold it for a variable time t, and finally ramp it down in 13 ms to acquire the TOF image. We verify that the average winding number decay is the same whether the obstacle is ramped up after 30 ms or 300 ms. To maximize the vortex visibility in the ring, we abruptly switch off the vertical trap, and we turn off the in-plane ring confinement with a 1-ms linear ramp. We then let the gas freely expand for another 0.5 ms before absorption imaging. To image vortices in the BCS superfluids, we use the same procedure described in Ref. [62], employing the trap release already mentioned.

We note that the measured N_v^{tot} is systematically lower than $\langle w_0 \rangle - \langle w_F \rangle$ [see Figs. 4(a) and 4(c)]. We mainly ascribe such discrepancy to the technical limitations of the experimental procedure to detect vortices: The 13-ms removal of the defect is likely to perturb the vortex dynamics, especially in the high-N_v regime [54]. Furthermore, we cannot exclude that the different boundary conditions at the inner ring radius of the geometries with and without the inner disk could affect the vortex emission. Finally, we want to stress that, once emitted, vortices leave the superfluid ring density much faster than the one introduced by the imprinting pulse, which are observed to survive on top of the current for several hundreds of ms. It is likely that the presence of the defect could accelerate the vortex escape after the completion of one entire loop, especially at the finite temperature of the experimental superfluid.

APPENDIX B: THEORETICAL METHODS

1. Numerical simulation of the phase imprinting

We perform simulations in the molecular BEC limit by numerically solving the time-dependent mean-field 3D GPE at $T = 0$ [47]. We employ a harmonic 3D potential with a tight confinement along the z direction and a hard-wall potential in the x-y plane to create the homogeneous ring trap, using the experimental parameters. The ground-state wave function is found by solving the GPE in imaginary time. To simulate the phase imprinting, we multiply the initial wave function by the phase factor $\exp\left(-i\Delta\phi_I(\theta)\right)$,
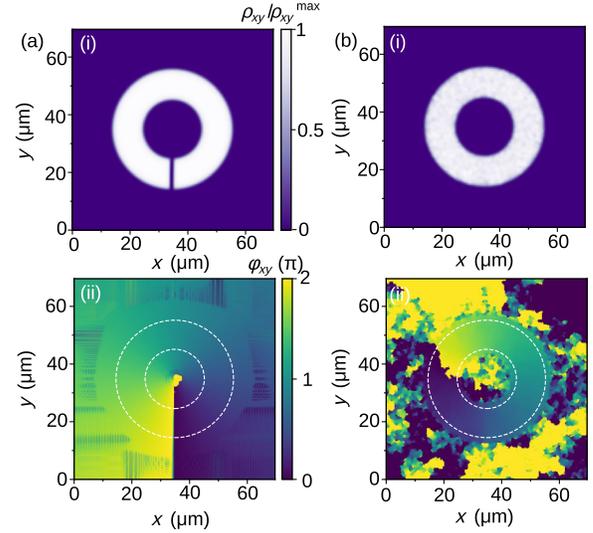
FIG. 7. Superfluid density (i), normalized to its maximum value, and its phase (ii) in the x, y plane at $z = 0$: (a) immediately after the imprinting of $\Delta\phi_I = 2\pi$, and (b) after 1-s evolution time. The density depletion in (a-i) is due to the finite width of the imprinting potential step. The dashed white circles in the phase profiles indicate the ring edges, where the superfluid density takes its bulk value.

with $\Delta\phi_I(\theta) = U(\theta)t_I/\hbar$. In order to model the imprinting potential, $U(\theta)$ is chosen to have the same azimuthal profile as used in the experiment [Fig. 2(c)]. Throughout our studies, we keep the peak value of the imprinting potential fixed and equal to the experimental value of 7.8 μ, where $\mu = 1.06$ kHz is the numerical chemical potential [47], and we vary the imprinting time to access different winding number w. We find that a time $t_I = 127.4$ µs is necessary to imprint a total phase of $\Delta\phi_I = 2\pi$, i.e., to excite $w = 1$, which is consistent with the experimental results in the BEC regime. In Fig. 7, we show the corresponding x-y plane condensate density ρ_{xy} and phase ϕ_{xy} at equilibrium [panel (a)] and 1 s after the imprinting [panel (b)], extracted from the Madelung representation of the wave function $\psi(r, \theta) = \sqrt{\rho(r, \theta)} \exp\left(i\phi(r, \theta)\right)$. Consistently with the experimental observations, the condensate density presents a depletion immediately after the imprinting, but it quickly decays in a few ms, leaving only some density fluctuations in the condensate density after 1 s evolution. A detailed study of the excitations introduced by the imprinting is reported in the Supplemental Material [47]. The 2D phase profile clearly shows the presence of a 2π jump at both times, indicating that a persistent current of $w = 1$ is imprinted. We note that initially the phase jump overlaps exactly with the density cut, while at $t = 1$ s it is located at a different angular position because of the superfluid rotation.

In order to directly compare the numerical and the experimental data, we implement the same experimental
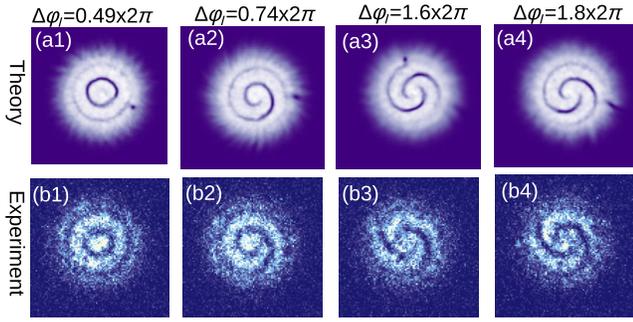
FIG. 8. Comparison between (a) numerical and (b) experimental BEC interferograms for different imprinted phases $\Delta\phi_I$ (see upper labels), corresponding to the imprinting times: (a1, b1) $t_I = 64$ μs, (a2, b2) $t_I = 96$ μs, (a3, b3) $t_I = 204$ μs, and (a4, b4) $t_I = 230$ μs. Both numerical and experimental interferograms are acquired after an evolution of 60 ms.

interferometric technique. We obtain numerical interferograms by quickly removing the ring boundaries in less than 1 ms and letting the ring and disk condensates interfere. For increasing imprinting time, and thus imprinted phase, we observe the numerical interferograms to change as shown in Fig. 8, where they are compared with experimental interferograms acquired for the BEC superfluid under the

same imprinting conditions. When we imprint a nonzero phase $\Delta\phi_I < \pi$, the interferograms show almost circularly concentric rings (a1), which characterizes the $w_0 = 0$ state. In this case, the numerical interferogram reveals the presence of a vortex, which carries the imprinted angular momentum. By further increasing $\Delta\phi_I$, we observe that the $w = 1$ or $w = 2$ persistent currents can be excited even for $\Delta\phi_I < 2\pi$ [(a2)-(b2)] or $\Delta\phi_I < 2 \times 2\pi$ [(a3)-(b3),(a4)-(b4)], respectively, and vortices or antivortices resulting from the decay of the initial density depletion are also involved to balance the imprinted angular momentum. The simulated interferograms match the experimentally recorded ones well and clearly show the presence of vortices for imprinted phases $\Delta\phi_I \neq 2\pi w$, with $|w| = 0$, 1, 2. Such vortices are also visible in experiments, but their unambiguous identification on top of interference fringes is difficult.

2. GPE simulation of the defect-induced current decay

We extend the 3D GPE numerical study at $T = 0$ to simulate the defect-induced current decay under the experimental condition of Sec. V. The studies in this section are performed by imprinting an ideal phase gradient to our initial condensate state, in order to avoid any density
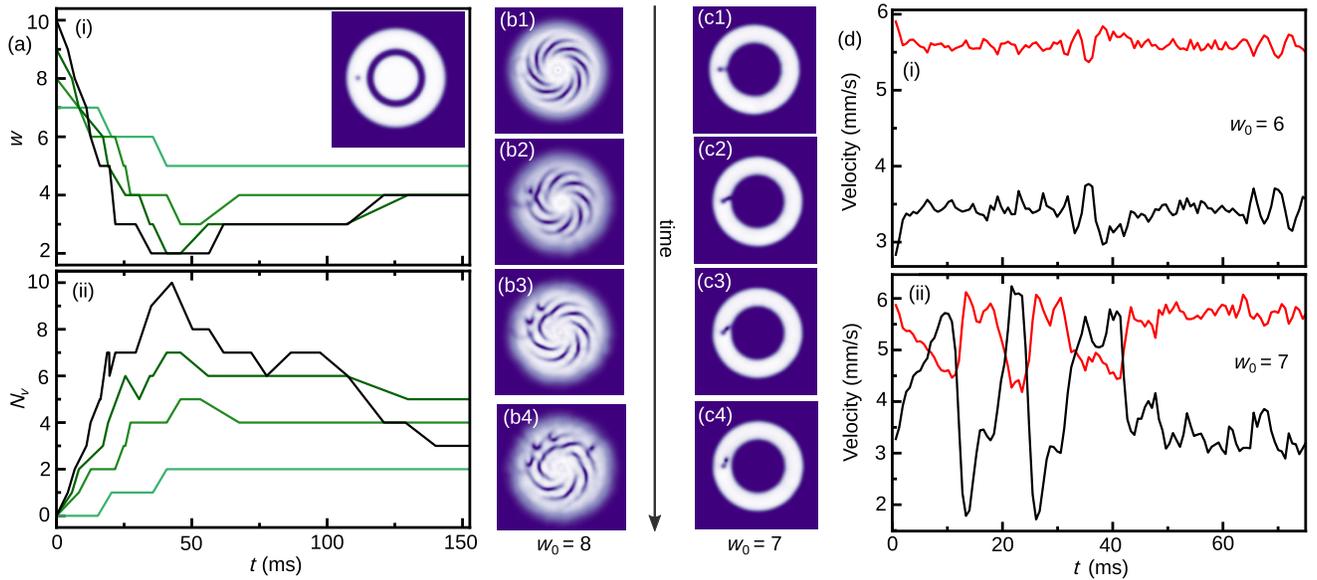
FIG. 9. Numerical study of the current decay in the presence of a local defect. (a) Time evolution of the winding number (i) and of the number of emitted vortices for different circulation states in the range $6 < w_0 \leq 10$. By employing the confining geometry shown in the inset, we compute the numerical interferograms to extract w and N_v. Here, the same color convention of Fig. 4 is used. (b1)–(b4) Numerical interferograms obtained at different times during the vortex emission process for an imprinted circulation $w_0 = 8$. The spiral arms give information about the winding number w; the dots instead indicate the vortices. The interferograms are extracted at $t = 0.3$ ms (b1: $w = 8$, $N_v = 0$), $t = 8.9$ ms (b2: $w = 7$, $N_v = 1$), $t = 13.4$ ms (b3: $w = 6$, $N_v = 2$), and $t = 28.0$ ms (b4: $w = 4$, $N_v = 4$). (c1)–(c4) The 2D density profiles in the x-y plane of the superfluid with the obstacle, close to the instant the first vortex is emitted for $w_0 = 7$, corresponding to (c1) $t = 9.6$ ms, (c2) $t = 12.7$ ms, (c3) $t = 13.4$ ms, and (c4) $t = 14.0$ ms. (d) Time evolution of the local superfluid velocity (black line) and the local speed of sound (red line) extracted at r_* for the imprinted circulation of (i) $w_0 = 6 = w_c$ and (ii) $w_0 = 7$. The vertical dashed gray lines for $w_0 = 7$ indicate the moments the vortices crossed the low-density channel, i.e., (c3) for the first emission.

excitations from the imprinting procedure. In the absence of the defect, the current produced with such an imprinting method is observed to be stable for all the investigated $w_0 \leq 10$. As the defect size is at the limit of the experimental resolution, it is hard to precisely know its height. For this reason, we numerically study the decay of the persistent current for different defect heights close to the experimental $V_0 \approx \mu$ in the BEC superfluid, which correspond to $V_0/E_F \simeq 0.1$, and we find the value of $V_0/\mu = 0.96$ to better fit both the experimental $\langle w \rangle$ decay and the average number of emitted vortices. Simulations at different $V_0/\mu \in [0.9, 4]$ show that this parameter affects mainly Γ and N_v of the current decay, whereas w_c barely depends on the obstacle height, changing only from 6 to 5 in the explored range. In the following, we show only our studies for $V_0/\mu = 0.96$ relevant for the comparison with the experiment.

Figure 9(a) shows the time evolution of the winding number w and of the number of emitted vortices N_v for $w_0 > w_c = 6$, where $w_0 = 7, 8$ profiles are the ones shown in Fig. 4(a). All reported numerical data are fitted to provide the data reported as shaded regions in Figs. 4(c)–4(e). In GPE simulations, we find two critical circulation values: The first one, $w_c = 6$, indicates the onset of dissipation, which happens through phase slippage caused by vortices entering from the inner edge of the ring. If we further increase w_0, we exceed a second critical value $w_{c2} = 8$ such that for $w_0 > w_{c2}$ antivortices (of opposite charge with respect to the winding number) could also be emitted into the superfluid. The interactions of vortices with antivortices, but also with other vortices or sound waves, cause annihilations or vortices and antivortices to leave the bulk, leading to the N_v decrease in time. For $w_c < w_0 < w_{c2}$, the vortex number instead remains constant to its maximum value. Following the interferograms in time, as shown for $w_0 = 8$ in Figs. 9(b1)–9(b4), we note that as the total number of vortices increases, the winding number decreases in time by keeping their sum equal to w_0. The relation $N_v^{\text{tot}} = w_0 - w_F$ remains a good approximation even for higher w_0, as shown in Fig. 4(c). We note that the curves at $w_0 > 7$ are not monotonically decreasing in time, but they all present a unit increment of w at $t \simeq 50$ ms, and those at $w_0 > 8$ also present a second one at $t \simeq 100$ ms. Here, the numerical images show a vortex leaving the superfluid density towards the center of the ring, after the interaction with other vortices and density excitations, and a consequent increase of w by one quantum. Such an effect happens only for high w_0, when a large number of vortices is emitted, and it is also observable in the darkest green data set of Fig. 4(a). The experimental shot-to-shot fluctuations are too large to provide a conclusive demonstration of such a vortex expulsion.

In order to give further insight into the microscopic description of the vortex emission process, we extract the 2D density of the superfluid in the x-y plane and follow it in

time around the instant when the first vortex is emitted, as shown in Fig. 9 for $w_0 = 7$. We find that for the considered defect height, vortices enter the superfluid from the inner edge of the ring, where its velocity is larger, and close to the defect position. In fact, a channel at low density is generated between the defect and the inner ring, which favors the entrance of the vortex from the very-low-density central region [Figs. 9(c1) and 9(c2)]. Then, this vortex propagates in the ring superfluid, and after some time, another one is emitted. These vortices travel in a loop in the superfluid, and after less than 100 ms, they return to the defect position, spiral around it, and then continue their propagation, as shown in the movie provided in the Supplemental Material [47]. For $w_0 > w_{c2}$, the vortex emission process becomes more complicated.

We then extract the superfluid velocity field as $\mathbf{v} = \mathbf{j}/n$ where $\mathbf{j}$ is the current density and n the superfluid density. We calculate its modulus value in the x-y plane at the midpoint between the defect and inner ring radius r_*, and we compare it to the local speed of sound $c = \sqrt{gn(r_*)/M}$. The temporal profiles of both v and c are shown in Fig. 9(d) for two examples: (i) $w_0 = 6$ and (ii) $w_0 = 7$. The value of c at r_* is close to the bulk value c_s of 5.8 mm/s even though it varies in time due to the density excitations. We observe that in both cases, there is an initial acceleration of the superfluid due to the constriction created between the defect and the inner edge of the ring. While for $w_0 = 6$ the acceleration stops almost immediately and v always remains smaller than c, for $w_0 = 7$, the superfluid instead continues accelerating until it achieves a maximum value exceeding the local speed of sound. This corresponds to the moment the linking low-density channel is created [Fig. 9(c1)]. After that, a vortex enters the condensate; it causes a phase slip and thus a jump in the superfluid velocity. The local minima of v correspond to the instants at which vortices depart from the region nearby the defect [Fig. 9(c3)]. Thus, the superfluid velocity shows discrete jumps in its profile induced by phase slippage due to vortex emission, similar to the findings in superfluid helium [67,68] and atomic Josephson junctions [54]. If we consider the initial superfluid velocity for $w_0 = w_c = 6$ at the ring's inner edge as the critical value for vortex nucleation, we find it to be smaller than both the bulk speed of sound, $c_s = 5.8$ mm/s, and the effective speed of sound obtained by averaging along the z axis, $c = 4.74$ mm/s.

Only for the first two peaks of Fig. 9(d-ii) does a vortex enter the bulk superfluid, while for the third one, it does not have enough energy to do so. In fact, the first two peaks are characterized by a sharp jump following the vortex emission into the superfluid. The vortex emission shows a periodic character, and even for the more complicated emission of $w_0 = 10$, Γ scales linearly with $w_0 - w_c$ as described in Fig. 4. We note a small shift of a few ms in the vortex emission time between panels (a) and (d) of Fig. 9,

due to some differences in the boundary conditions with [(a)] and without [(b)] the central disk [47].

APPENDIX C: DENSITY PERTURBATIONS INTRODUCED BY THE PHASE IMPRINTING

As mentioned in the main text, the phase imprinting introduces density excitations in correspondence with the gradient discontinuity. To characterize these excitations, we monitor the *in situ* density profile of the ring superfluid at short times after the imprinting procedure. In particular, in correspondence with the maximum of the imprinting gradient, the atomic density is observed to present both a depletion and an accumulation of atoms close to each other [Fig. 10(a)], as a result of the action of the sharp antigradient in the opposite direction. In fact, during the imprinting, such an antigradient imparts a large momentum kick to the portion of atoms that it illuminates, creating both a density accumulation and depletion next to each other. For increasing time after the imprinting, the density depletion and the accumulation are observed to travel in opposite directions with different velocities while progressively reducing their amplitude until they are not visible anymore [Fig. 10(a)]. We quantitatively characterize such a behavior by fitting the integrated profile of the
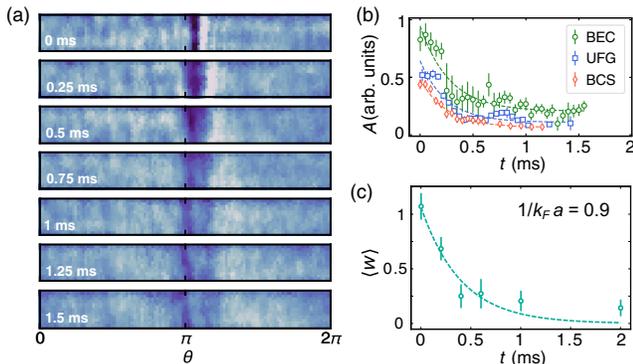
FIG. 10. Short-timescale dynamics after the imprinting. (a) Time evolution of the *in situ* density profile of a BEC superfluid after a $\Delta\phi_I \simeq 2\pi$ imprinting. Each image consists of an average of 10 absorption images, changed into polar coordinates. (b) Amplitude of the density depletion as a function of time after the suited imprinting pulse to populate the $w = 1$ state in the three interaction regimes (see legend). Each data point corresponds to the fitted value and 1σ uncertainty from a gaussian fit of the integrated density. For UFG and BCS they are obtained from the analysis of the *in situ* superfluid density with no magnetic field sweep. Each curve is fitted with an exponential function providing a decay time of $\tau = \{0.28(5), 0.25(5), 0.25(3)\}$ ms in the BEC, UFG and BCS regime, respectively. (c) Short-time dynamics of the average winding number and its SEM after an imprinting of $\Delta\phi_I = 2\pi$ in a strongly interacting superfluid at $1/k_F a \simeq 0.9$, measured from the interferograms acquired at the same interaction strength. The dashed line represents an exponential fit of the data with $\tau = 400(80)$ μs.

accumulation and depletion with two independent Gaussian functions. By analyzing the *in situ* density profiles after the imprinting pulse suited to excite the $w = 1$ current state, we find that the accumulation travels at a velocity consistent with the speed of sound in each of the three interaction regimes, whereas the depletion proceeds at a fraction of c_s, i.e., at $\simeq \{50\%, 15\%, 40\%\} c_s$ in the BEC, UFG, and BCS regimes, respectively. These values are consistent with a soundlike nature of the accumulation and a gray solitonlike nature of the depletion, despite the latter not necessarily possessing the soliton phase profile. In fact, the depletion is observed in the *in situ* density profile after the imprinting of any $\Delta\phi_I \gtrsim \pi$ for all interaction regimes, but only for $\Delta\phi_I = \pi + 2n\pi$, with integer n, is it equipped with the proper phase profile of a soliton. Both the sound and the solitonlike excitations are observed to exponentially reduce their amplitude to completely disappear from the density profile in a few-ms timescale, as reported in Fig. 10(b) for the latter. A similar behavior is also observed in the GPE numerical simulation of the experimental imprinting profile [47]. In particular, when $\Delta\phi_I = \pi$, the decay dynamics of the density depletion resemble that observed for solitons [69,70]: It undergoes a snaking instability and eventually decays into a vortex or antivortex. For different imprinted phases, the depletion decay dynamics changes, but it always eventually produces a number of vortices that depend on the applied $\Delta\phi_I$. Those imprinting vortices are then observed to survive on top of the excited current without significantly perturbing it.

In order to understand the possible detrimental effect of these perturbations on the superfluid circulation state, especially in the strongly interacting regime, which presents a shift on the $\langle w \rangle - \Delta\phi_I$ curve [Fig. 3(a)], we compare the density excitations dynamics with the short-timescale evolution of the interferograms. In the BEC superfluid, we observe that the spiral pattern of the fringes is present in the interferograms even at the shortest time after the imprinting we can probe, corresponding to the sole 1.2 ms of the TOF, and that the $\langle w \rangle - \Delta\phi_I$ curve of Fig. 3(a) is independent on the time at which we probe. These observations demonstrate the negligible effect of the density excitations introduced by the imprinting on the current in the BEC regime. On the other hand, the 50-ms magnetic field ramp needed to acquire interferograms in the UFG and BCS regimes prevents us from exploring the short-timescale dynamics of their interferograms. To investigate the role of the density excitations in strongly interacting superfluids, we therefore focus on the most strongly interacting BEC ($1/k_F a = 0.9$) that still shows clear interferograms with no need for sweeping the magnetic field and yet presents a sensible shift in the $\langle w \rangle - \Delta\phi_I$ curve [see Fig. 3(a) inset]. The time evolution of $\langle w \rangle$ after an imprinting of $\Delta\phi_I = 2\pi$ in such a regime is reported in Fig. 10(c): The 2π phase winding is effectively imprinted, but it quickly decays in a few-ms timescale, without giving

rise to a persistent current. The comparable timescales of the phase winding decay and of the density excitations introduced by the imprinting hints at a connection between the two, as confirmed by the fact that when a barrier is added on the imprinting profile to avoid the density excitations, no decay is detected in the current after the imprinting of 2π. The polluting effect of the antigradient on the imprinted circulation produces a more dramatic effect on strongly interacting superfluids, which, as for the case of soliton imprinting [52], appear to be more sensitive to the sharpness of the imprinted profile. In the future, it would be interesting to investigate further the effect of the imprinting profile on strongly interacting superfluids, both from an experimental and a theoretical point of view.

---

[1] N. Byers and C. N. Yang, *Theoretical Considerations Concerning Quantized Magnetic Flux in Superconducting Cylinders*, Phys. Rev. Lett. **7**, 46 (1961).

[2] F. Bloch, *Off-Diagonal Long-Range Order and Persistent Currents in a Hollow Cylinder*, Phys. Rev. **137**, A787 (1965).

[3] B. S. Deaver and W. M. Fairbank, *Experimental Evidence for Quantized Flux in Superconducting Cylinders*, Phys. Rev. Lett. **7**, 43 (1961).

[4] R. Doll and M. Näbauer, *Experimental Proof of Magnetic Flux Quantization in a Superconducting Ring*, Phys. Rev. Lett. **7**, 51 (1961).

[5] L. Onsager, *Magnetic Flux Through a Superconducting Ring*, Phys. Rev. Lett. **7**, 50 (1961).

[6] H. Bluhm, N. C. Koshnick, J. A. Bert, M. E. Huber, and K. A. Moler, *Persistent Currents in Normal Metal Rings*, Phys. Rev. Lett. **102**, 136802 (2009).

[7] A. C. Bleszynski-Jayich, W. E. Shanks, B. Peaudecerf, E. Ginossar, F. von Oppen, L. Glazman, and J. G. E. Harris, *Persistent Currents in Normal Metal Rings*, Science **326**, 272 (2009).

[8] M. Tinkham, *Introduction to Superconductivity* (Dover Publications, Inc., Mineola, NY, 2004).

[9] J. Dalibard, F. Gerbier, G. Juzeliunas, and P. Öhberg, *Colloquium: Artificial Gauge Potentials for Neutral Atoms*, Rev. Mod. Phys. **83**, 1523 (2011).

[10] N. Goldman, G. Juzeliūnas, P. Öhberg, and I. B. Spielman, *Light-Induced Gauge Fields for Ultracold Atoms*, Rep. Prog. Phys. **77**, 126401 (2014).

[11] Y. Aharonov and D. Bohm, *Significance of Electromagnetic Potentials in the Quantum Theory*, Phys. Rev. **115**, 485 (1959).

[12] A. Kadin, *Introduction to Superconducting Circuits* (Wiley, New York, 1999).

[13] A. J. Leggett, *Superfluidity*, Rev. Mod. Phys. **71**, S318 (1999).

[14] E. J. Mueller, *Superfluidity and Mean-Field Energy Loops: Hysteretic Behavior in Bose-Einstein Condensates*, Phys. Rev. A **66**, 063603 (2002).

[15] F. Bloch, *Superfluidity in a Ring*, Phys. Rev. A **7**, 2187 (1973).

[16] C. Ryu, M. F. Andersen, P. Clade, V. Natarajan, K. Helmerson, and W. D. Phillips, *Observation of Persistent Flow of a Bose-Einstein Condensate in a Toroidal Trap*, Phys. Rev. Lett. **99**, 260401 (2007).

[17] S. Moulder, S. Beattie, R. P. Smith, N. Tammuz, and Z. Hadzibabic, *Quantized Supercurrent Decay in an Annular Bose-Einstein Condensate*, Phys. Rev. A **86**, 013629 (2012).

[18] S. Beattie, S. Moulder, R. J. Fletcher, and Z. Hadzibabic, *Persistent Currents in Spinor Condensates*, Phys. Rev. Lett. **110**, 025301 (2013).

[19] K. C. Wright, R. B. Blakestad, C. J. Lobb, W. D. Phillips, and G. K. Campbell, *Driving Phase Slips in a Superfluid Atom Circuit with a Rotating Weak Link*, Phys. Rev. Lett. **110**, 025302 (2013).

[20] A. Kumar, S. Eckel, F. Jendrzejewski, and G. K. Campbell, *Temperature-Induced Decay of Persistent Currents in a Superfluid Ultracold Gas*, Phys. Rev. A **95**, 021602(R) (2017).

[21] Y. Cai, D. G. Allman, P. Sabharwal, and K. C. Wright, *Persistent Currents in Rings of Ultracold Fermionic Atoms*, Phys. Rev. Lett. **128**, 150401 (2022).

[22] R. Dubessy, T. Liennard, P. Pedri, and H. Perrin, *Critical Rotation of an Annular Superfluid Bose-Einstein Condensate*, Phys. Rev. A **86**, 011602(R) (2012).

[23] J. Polo, R. Dubessy, P. Pedri, H. Perrin, and A. Minguzzi, *Oscillations and Decay of Superfluid Currents in a One-Dimensional Bose Gas on a Ring*, Phys. Rev. Lett. **123**, 195301 (2019).

[24] M. Kunimi and I. Danshita, *Decay Mechanisms of Superflow of Bose-Einstein Condensates in Ring Traps*, Phys. Rev. A **99**, 043613 (2019).

[25] Z. Mehdi, A. S. Bradley, J. J. Hope, and S. S. Szigeti, *Superflow Decay in a Toroidal Bose Gas: The Effect of Quantum and Thermal Fluctuations*, SciPost Phys. **11**, 80 (2021).

[26] E. E. Ferrero, L. Foini, T. Giamarchi, A. B. Kolton, and A. Rosso, *Creep Motion of Elastic Interfaces Driven in a Disordered Landscape*, Annu. Rev. Condens. Matter Phys. **12**, 111 (2021).

[27] L. Amico, M. Boshier, G. Birkl, A. Minguzzi, C. Miniatura, L.-C. Kwek, D. Aghamalyan, V. Ahufinger, D. Anderson, N. Andrei *et al.*, *Roadmap on Atomtronics: State of the Art and Perspective*, AVS Quantum Sci. **3**, 039201 (2021).

[28] L. Amico, D. Anderson, M. Boshier, J.-P. Brantut, L.-C. Kwek, A. Minguzzi, and W. von Klitzing, *Colloquium: Atomtronic Circuits: From Many-Body Physics to Quantum Technologies*, Rev. Mod. Phys. **94**, 041001 (2022).

[29] D. Aghamalyan, M. Cominotti, M. Rizzi, D. Rossini, F. Hekking, A. Minguzzi, L.-C. Kwek, and L. Amico, *Coherent Superposition of Current Flows in an Atomtronic Quantum Interference Device*, New J. Phys. **17**, 045023 (2015).

[30] A. Ramanathan, K. C. Wright, S. R. Muniz, M. Zelan, W. T. Hill III, C. J. Lobb, K. Helmerson, W. D. Phillips, and G. K. Campbell, *Superflow in a Toroidal Bose-Einstein Condensate: An Atom Circuit with a Tunable Weak Link*, Phys. Rev. Lett. **106**, 130401 (2011).

[31] C. Ryu, P. W. Blackburn, A. A. Blinova, and M. G. Boshier, *Experimental Realization of Josephson Junctions for an Atom SQUID*, Phys. Rev. Lett. **111**, 205301 (2013).

[32] S. Eckel, J. G. Lee, F. Jendrzejewski, N. Murray, C. W. Clark, C. J. Lobb, W. D. Phillips, M. Edwards, and G. K. Campbell, *Hysteresis in a Quantized Superfluid 'Atomtronic' Circuit*, Nature (London) **506,** 200 (2014).

[33] C. Ryu, E. Samson, and M. G. Boshier, *Quantum Interference of Currents in an Atomtronic SQUID*, Nat. Commun. **11,** 3338 (2020).

[34] H. Kiehn, V. P. Singh, and L. Mathey, *Implementation of an Atomtronic SQUID in a Strongly Confined Toroidal Condensate*, Phys. Rev. Res. **4,** 033024 (2022).

[35] T. L. Gustavson, P. Bouyer, and M. A. Kasevich, *Precision Rotation Measurements with an Atom Interferometer Gyroscope*, Phys. Rev. Lett. **78,** 2046 (1997).

[36] P. Navez, S. Pandey, H. Mas, K. Poulios, T. Fernholz, and W. von Klitzing, *Matter-Wave Interferometers Using TAAP Rings*, New J. Phys. **18,** 075014 (2016).

[37] S. Pandey, H. Mas, G. Drougakis, P. Thekkeppatt, V. Bolpasi, G. Vasilakis, K. Poulios, and W. von Klitzing, *Hypersonic Bose–Einstein Condensates in Accelerator Rings*, Nature (London) **570,** 205 (2019).

[38] S. Hofferberth, I. Lesanovsky, B. Fischer, T. Schumm, and J. Schmiedmayer, *Non-Equilibrium Coherence Dynamics in One-Dimensional Bose Gases*, Nature (London) **449,** 324 (2007).

[39] T. Schweigler, V. Kasper, S. Erne, I. Mazets, B. Rauer, F. Cataldini, T. Langen, T. Gasenzer, J. Berges, and J. Schmiedmayer, *Experimental Characterization of a Quantum Many-Body System via Higher-Order Correlations*, Nature (London) **545,** 323 (2017).

[40] S. Burger, K. Bongs, S. Dettmer, W. Ertmer, K. Sengstock, A. Sanpera, G. V. Shlyapnikov, and M. Lewenstein, *Dark Solitons in Bose-Einstein Condensates*, Phys. Rev. Lett. **83,** 5198 (1999).

[41] T. Yefsah, A. T. Sommer, M. J. Ku, L. W. Cheuk, W. Ji, W. S. Bakr, and M. W. Zwierlein, *Heavy Solitons in a Fermionic Superfluid*, Nature (London) **499,** 426 (2013).

[42] N. Luick, L. Sobirey, M. Bohlen, V. P. Singh, L. Mathey, T. Lompe, and H. Moritz, *An Ideal Josephson Junction in an Ultracold Two-Dimensional Fermi Gas*, Science **369,** 89 (2020).

[43] Y. Zheng and J. Javanainen, *Classical and Quantum Models for Phase Imprinting*, Phys. Rev. A **67,** 035602 (2003).

[44] S. Eckel, F. Jendrzejewski, A. Kumar, C. J. Lobb, and G. K. Campbell, *Interferometric Measurement of the Current-Phase Relationship of a Superfluid Weak Link*, Phys. Rev. X **4,** 031052 (2014).

[45] L. Corman, L. Chomaz, T. Bienaimé, R. Desbuquois, C. Weitenberg, S. Nascimbene, J. Dalibard, and J. Beugnon, *Quench-Induced Supercurrents in an Annular Bose Gas*, Phys. Rev. Lett. **113,** 135302 (2014).

[46] R. Mathew, A. Kumar, S. Eckel, F. Jendrzejewski, G. K. Campbell, M. Edwards, and E. Tiesinga, *Self-Heterodyne Detection of the in situ Phase of an Atomic Superconducting Quantum Interference Device*, Phys. Rev. A **92,** 033602 (2015).

[47] See Supplemental Material at http://link.aps.org/supplemental/10.1103/PhysRevX.12.041037 for further details on the experimental methods and the theoretical modeling tools.

[48] A. Pérez-Obiol, J. Polo, and L. Amico, *Coherent Phase Slips in Coupled Matter-Wave Circuits*, Phys. Rev. Res. **4,** L022038 (2022).

[49] T. Bland, Q. Marolleau, P. Comaron, B. Malomed, and N. Proukakis, *Persistent Current Formation in Double-Ring Geometries*, J. Phys. B **53,** 115301 (2020).

[50] G. Pelegrí, A. M. Marques, V. Ahufinger, J. Mompart, and R. G. Dias, *Second-Order Topological Corner States with Ultracold Atoms Carrying Orbital Angular Momentum in Optical Lattices*, Phys. Rev. B **100,** 205109 (2019).

[51] G. Pecci, P. Naldesi, L. Amico, and A. Minguzzi, *Probing the BCS-BEC Crossover with Persistent Currents*, Phys. Rev. Res. **3,** L032064 (2021).

[52] K. Sacha and D. Delande, *Proper Phase Imprinting Method for a Dark Soliton Excitation in a Superfluid Fermi Mixture*, Phys. Rev. A **90,** 021604(R) (2014).

[53] A. Kumar, R. Dubessy, T. Badr, C. De Rossi, M. de Goër de Herve, L. Longchambon, and H. Perrin, *Producing Superfluid Circulation States Using Phase Imprinting*, Phys. Rev. A **97,** 043615 (2018).

[54] K. Xhani, E. Neri, L. Galantucci, F. Scazza, A. Burchianti, K.-L. Lee, C. F. Barenghi, A. Trombettoni, M. Inguscio, M. Zaccanti, G. Roati, and N. P. Proukakis, *Critical Transport and Vortex Dynamics in a Thin Atomic Josephson Junction*, Phys. Rev. Lett. **124,** 045301 (2020).

[55] M. T. Reeves, T. P. Billam, B. P. Anderson, and A. S. Bradley, *Identifying a Superfluid Reynolds Number via Dynamical Similarity*, Phys. Rev. Lett. **114,** 155302 (2015).

[56] W. J. Kwon, S. W. Seo, and Y.-i. Shin, *Periodic Shedding of Vortex Dipoles from a Moving Penetrable Obstacle in a Bose-Einstein Condensate*, Phys. Rev. A **92,** 033613 (2015).

[57] J. W. Park, B. Ko, and Y.-i. Shin, *Critical Vortex Shedding in a Strongly Interacting Fermionic Superfluid*, Phys. Rev. Lett. **121,** 225301 (2018).

[58] T. Giamarchi, *Current Drag in Two Leg Quantum Ladders*, Physica (Amsterdam) **77E,** 164 (2016), Frontiers in Quantum Electronic Transport—In memory of Markus Büttiker.

[59] I. Chestnov, A. Yulin, I. A. Shelykh, and A. Kavokin, *Dissipative Josephson Vortices in Annular Polariton Fluids*, Phys. Rev. B **104,** 165305 (2021).

[60] J. Mooij and C. Harmans, *Phase-Slip Flux Qubits*, New J. Phys. **7,** 219 (2005).

[61] S. Ragole and J. M. Taylor, *Interacting Atomic Interferometry for Rotation Sensing Approaching the Heisenberg Limit*, Phys. Rev. Lett. **117,** 203002 (2016).

[62] W. Kwon, G. Del Pace, K. Xhani, L. Galantucci, A. Muzi Falconi, M. Inguscio, F. Scazza, and G. Roati, *Sound Emission and Annihilations in a Programmable Quantum Vortex Collider*, Nature (London) **600,** 64 (2021).

[63] R. Combescot, M. Y. Kagan, and S. Stringari, *Collective Mode of Homogeneous Superfluid Fermi Gases in the BEC-BCS Crossover*, Phys. Rev. A **74,** 042717 (2006).

[64] W. Weimer, K. Morgener, V. P. Singh, J. Siegl, K. Hueck, N. Luick, L. Mathey, and H. Moritz, *Critical Velocity in the BEC-BCS Crossover*, Phys. Rev. Lett. **114,** 095301 (2015).

[65] W. Ketterle and M. W. Zwierlein, *Making, Probing and Understanding Ultracold Fermi Gases*, in *Ultra-Cold*

Fermi Gases, edited by M. Inguscio, W. Ketterle, and C. Salomon (IOS Press, Amsterdam, 2008), Vol. 164, pp. 95–287.

[66] W. J. Kwon, G. Del Pace, R. Panza, M. Inguscio, W. Zwerger, M. Zaccanti, F. Scazza, and G. Roati, *Strongly Correlated Superfluid Order Parameters from dc Josephson Supercurrents*, Science **369**, 84 (2020).

[67] E. Hoskinson, Y. Sato, I. Hahn, and R. E. Packard, *Transition from Phase Slips to the Josephson Effect in a Superfluid* ⁴He *Weak Link*, Nat. Phys. **2**, 23 (2006).

[68] Y. Sato and R. E. Packard, *Superfluid Helium Quantum Interference Devices: Physics and Applications*, Rep. Prog. Phys. **75**, 016401 (2012).

[69] S. Donadello, S. Serafini, M. Tylutki, L. P. Pitaevskii, F. Dalfovo, G. Lamporesi, and G. Ferrari, *Observation of Solitonic Vortices in Bose-Einstein Condensates*, Phys. Rev. Lett. **113**, 065302 (2014).

[70] M. J. H. Ku, B. Mukherjee, T. Yefsah, and M. W. Zwierlein, *Cascade of Solitonic Excitations in a Superfluid Fermi Gas: From Planar Solitons to Vortex Rings and Lines*, Phys. Rev. Lett. **116**, 045304 (2016).